

Supplemental Materials for “Origins of Ultralow Thermal Conductivity in Bulk [6,6]-Phenyl-C₆₁-Butyric Acid Methyl Ester (PCBM)”

Jan-Hendrik Pöhls^a, Michel B. Johnson^b, Mary Anne White^{a,b,c,*}

^a Department of Physics and Atmospheric Science, Dalhousie University, Halifax, NS B3H 4R2, Canada

^b Institute for Research in Materials, Dalhousie University, Halifax, NS B3H 4R2, Canada

^c Department of Chemistry, Dalhousie University, Halifax, NS B3H 4R2, Canada

* Corresponding author: Mary Anne White, mary.anne.white@dal.ca

X-Ray Diffraction

The PXRD pattern of as-received PCBM powder and a consolidated pellet are shown in Figure S1. No new peaks or shifts in peaks were observed, indicating that consolidation did not distort the structure. The recorded PXRD patterns are similar to the patterns reported for PCBM thin films [1,2] and PCBM powder [3]. However, Mens *et al.* stated that the ability of PCBM to have different morphologies depends on the preparation methods [4]. While their recorded patterns on PCBM powder indicate smaller crystals with amorphous regions, the present PCBM powder and pellet were both highly crystalline with large crystals.

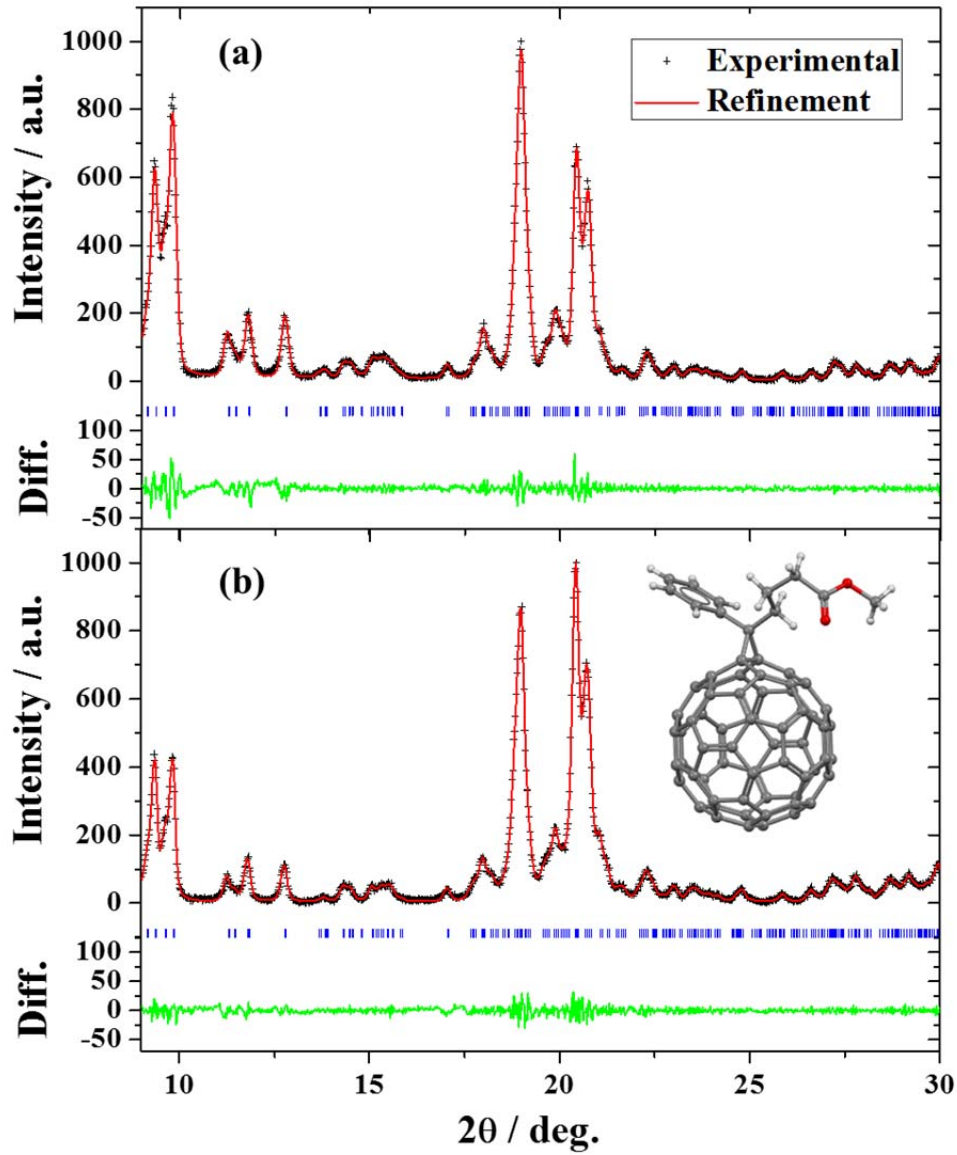


FIG. S1: PXRd pattern of PCBM powder and consolidated PCBM pellets. Le Bail refinements of (a) PCBM powder and (b) PCBM pellet indicate a reduction in unit cell volume with applied pressure. (The refinement data are given in Table S1.) Inset: PCBM molecular structure (\bullet : carbon atom; \bullet : oxygen atom; \circ : hydrogen atom).

Table S1: Results from XRD data for PCBM powder and PCBM pellet refined using the Le Bail method. The lattice constant a and the angle β changed slightly with pelletizing while the lattice constants b and c were almost constant.

Parameter	PCBM Powder	PCBM Pellet
Space group	$P2_1/n$ (No. 14)	$P2_1/n$ (No. 14)
$a / \text{\AA}$	13.529	13.503
$b / \text{\AA}$	15.203	15.199
$c / \text{\AA}$	19.117	19.119
$\alpha / ^\circ$	90.000	90.000
$\beta / ^\circ$	106.960	107.013
$\gamma / ^\circ$	90.000	90.000
Number of molecules per unit cell, Z	4	4
Volume / \AA^3	3761	3752
Calculated density / (g cm^{-3})	1.609	1.613
R_p	4.950	4.512
R_{wp}	8.121	8.816
χ^2	0.604	0.676

Raman Spectroscopy

In the absence of published PCBM Raman spectra over the full frequency range, the Raman spectra were compared to C_{60} powder (>99.5%; Sigma Aldrich; Fig. 2 (c)) [5]. C_{60} has 10 Raman modes (2 A_g and 8 H_g) and 4 infrared modes (4 F_{1u}) which are highly degenerate due to its high symmetry (I_h). However, in PCBM the icosahedral modes in the fcc structure of C_{60} are split into a partially broken symmetry (C_{2v}) for the fullerene core, resulting in an increased number of Raman peaks in PCBM (Fig. 2) [6]. A shift to lower wavenumbers of the $A_g(2)$ peak on going from C_{60} to PCBM was observed (Table S2), due to the increased negative charge on the fullerene core due to its high electron acceptor potential [7]. A DFT calculation of the Raman spectrum of PCBM [8] does not fully represent the measured spectrum, but the present results do agree with experimental Raman spectra for thin films of PCBM in their region of overlap at high wavenumbers ($1400\text{-}1600\text{ cm}^{-1}$) [9]. Four major Raman peaks (88 cm^{-1} , 348 cm^{-1} , 521 cm^{-1} , and 1001 cm^{-1} ; black arrows in Fig. 2) were recorded for PCBM. These modes are attributed to the side chain. The Raman peak at 1001 cm^{-1} is due to the breathing mode of the phenyl group [9] while the low-frequency Raman peaks are most likely due to rotation and carbon-carbon stretching of the butyric acid methyl ester group and the rotation of the phenyl group.

Table S2: Experimentally determined frequencies (in wavenumbers) of Raman peaks in C₆₀, PCBM powder, and a consolidated PCBM pellet.

C ₆₀ / cm ⁻¹ [5]	PCBM Powder / cm ⁻¹	PCBM Pellet / cm ⁻¹
	75	75
	88	88
	103	103
	163	163
	182	184
266	255	255
273 (<i>H_g</i> (1))	271	271
	348	348
433 (<i>H_g</i> (2))	429	429
496 (<i>A_g</i> (1))	481	483
	520	522
568	531	531
709 (<i>H_g</i> (3))	709	709
771 (<i>H_g</i> (4))	768	768
	776	778
1101 (<i>H_g</i> (5))	1104	1104
1251 (<i>H_g</i> (6))	1249	1251
1424 (<i>H_g</i> (7))	1424	1424
1469 (<i>A_g</i> (2))	1461	1463
1574 (<i>H_g</i> (8))	1573	1575

Ultralow Thermal Conductivity of C₆₀/C₇₀

The present minimum thermal conductivity model (see manuscript and Figure S2) was tested for PCBM and C₆₀/C₇₀ and compared with both the minimum Einstein thermal conductivity [10] and the minimum thermal conductivity model of Cahill *et al.* [11]. The heat capacity and thermal conductivity data for C₆₀/C₇₀ were taken from Olsen *et al.* [12]. The heat capacity of C₆₀/C₇₀ was fit as follows: one linear term in T ($a = 1.8 \text{ mJ mol}^{-1} \text{ K}^{-2}$), one Debye ($n_D = 0.25$, $\theta_D = 54.0 \text{ K}$), and four Einstein terms ($n_{E1} = 0.0833$, $\theta_{E1} = 14.0 \text{ K}$, $n_{E2} = 0.583$, $\theta_{E2} = 24.2 \text{ K}$, $n_{E3} = 0.333$, $\theta_{E3} = 39.8 \text{ K}$, $n_{E4} = 1.0$, $\theta_{E4} = 56.0 \text{ K}$) (Fig. S2 (c)). Figs. S2 (b) and (d) show that the present model fits the experimental thermal conductivities well for both PCBM and C₆₀/C₇₀ without any adjustable parameters. While the minimum Einstein thermal conductivity fits the

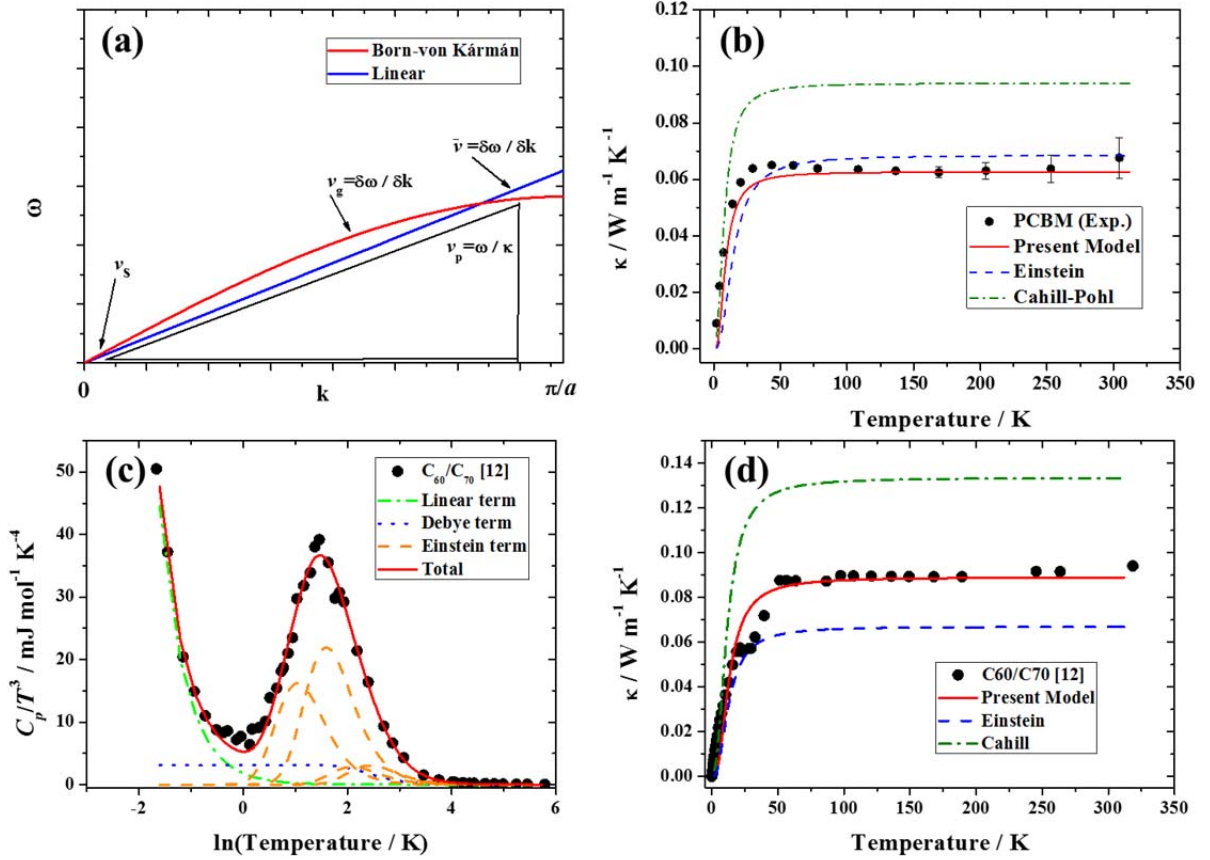


FIG. S2: (a) Dispersion diagrams: Debye assumed a linear dispersion in the first Brillouin zone while the dispersion curve in the Born-von Kármán model is curved. (b) Thermal conductivity of PCBM: The present minimum thermal conductivity model agrees well with the experimental thermal conductivity for PCBM. (c) Heat capacity of C_{60}/C_{70} : The heat capacity [12] was fit with a linear term, one Debye term, and four Einstein terms. (d) Thermal conductivity of C_{60}/C_{70} : Einstein, Cahill and present models compared with the experimental thermal conductivity of C_{60}/C_{70} [12].

experimental thermal conductivity of PCBM well, the Einstein model predicts a lower thermal conductivity for C_{60}/C_{70} compared to experiment. The minimum thermal conductivity model of Cahill *et al.* overestimates the thermal conductivity of both materials. It is important to note that the Einstein temperatures and Debye temperatures from the heat capacity fits were used for all models; using speed of sound would have led to a great difference between calculated thermal

conductivity and experimental data. The low Debye temperature in PCBM might be a result of low-frequency resonant modes as computed for methyl-doped silicon dioxide [13]. Recent molecular dynamic simulations show a low thermal conductivity of PCBM [14] but the experimental heat capacity results of PCBM at low temperature were lower than calculated from their phonon density of states. For the molecular dynamic simulations a simplified lattice was used (hexagonal with one molecule per unit cell, whereas the PCBM pellets have a monoclinic unit cell with four molecules per unit cell (Table S1)). An *ab initio* computational study of the monoclinic unit cell is currently not feasible due to its large unit cell with 352 atoms.

Thermal Expansion

The thermal conductivity of the PCBM pellet is proportional to the dimensions of the pellet and the atomic density. Dimensions and density can change due to thermal expansion/contraction. Our dilatometry results (Figure S3) show that the PCBM dimensions are nearly constant from 25 to 150 °C, followed by a dramatic increase between 180 °C and 210 °C. It is important to note that this high-temperature expansion is irreversible, most likely due to a change in the crystal structure (see below).

A similar expansion at this temperature range had been found for polymerized C₆₀ [15]. However, the PCBM pellets were consolidated at pressure lower than the polymerization pressure for C₆₀ and no change in PCBM space group and Raman spectra was observed with consolidation (Fig. S1 and Fig. 2), so polymerization of PCBM was ruled out.

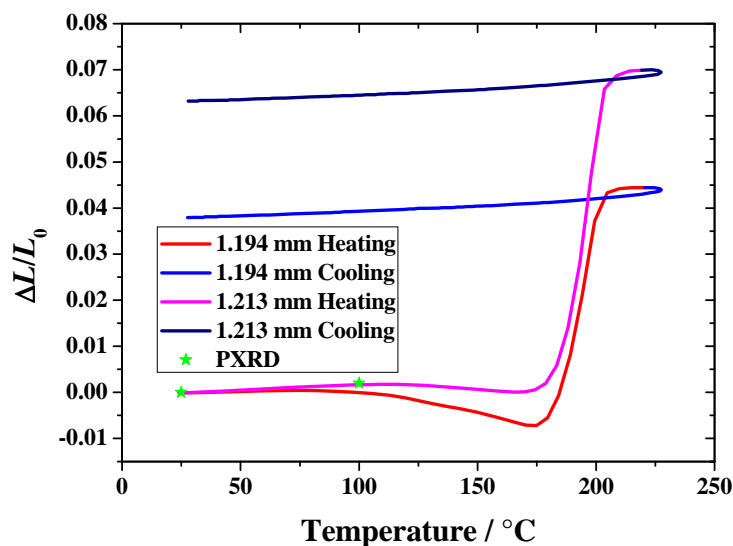


FIG. S3: Thermal expansion of two PCBM pellets of different thicknesses as indicated, determined by dilatometry. An irreversible expansion was observed between 180 and 210 °C. The thermal expansion results agree well with the change in volume as determined by PXR.

The thermal expansion results were confirmed by PXR results for a PCBM pellet determined at different temperature (123 K, 223 K, 298 K, 373 K, and 473 K). The intensity of the peaks increased with temperature and the peaks shifted to lower angles resulting in an increase in unit cell volume (see Fig. S4). Additional peaks were recorded at 473 K which confirms the high-temperature change in the crystal structure. The PXR patterns were refined by the Le Bail method and the data are given in Table S3. An increase in density from 150 K to 200 K had been calculated for solvent-free PCBM molecules in the monoclinic phase [16], but is not consistent with our data. Furthermore, the calculated density for their results is in the range of amorphous PCBM while the PCBM pellets show crystalline behavior at room temperature.

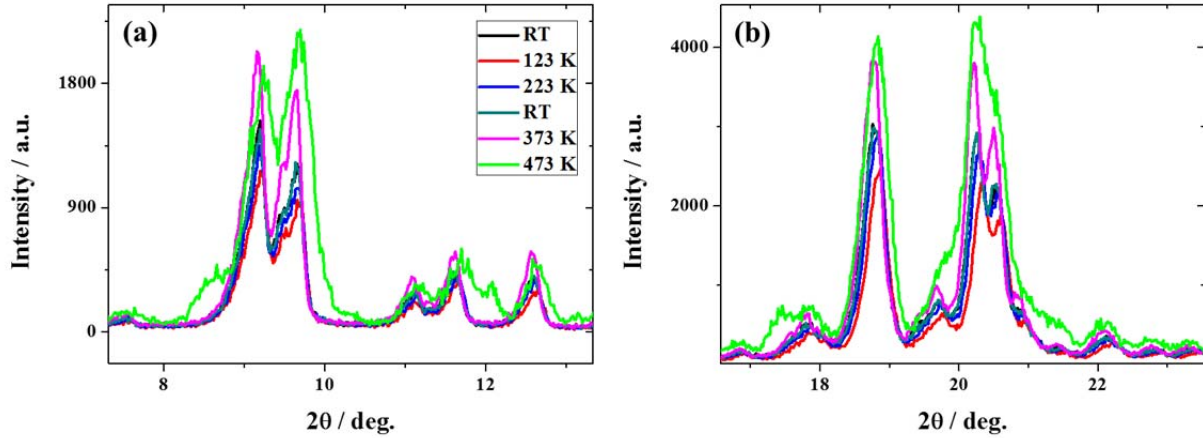


FIG. S4: PXRD at different temperatures (123 K, 223 K, 298 K, 373 K, and 473 K). The peak intensities increased with temperature. Additional peaks were observed at 473 K.

Table S3: Results of PXRD experiments for a PCBM pellet at several temperatures, from refinements using the Le Bail method. The PXRD at 473 K could not be refined due to a change in structure. The observed density decreases from 123 K to 223 K (volume coefficient of thermal expansion $\sim 3 \times 10^{-4} \text{ K}^{-1}$) and then stays constant to 373 K.

Parameter	123 K	223 K	300 K	373 K
Space group	$P2_1/n$ (No. 14)	$P2_1/n$ (No. 14)	$P2_1/n$ (No. 14)	$P2_1/n$ (No. 14)
$a / \text{\AA}$	13.423	13.538	13.512	13.530
$b / \text{\AA}$	15.148	15.299	15.265	15.270
$c / \text{\AA}$	18.954	19.153	19.139	19.153
$\alpha / ^\circ$	90.000	90.000	90.000	90.000
$\beta / ^\circ$	106.839	107.026	107.039	107.032
$\gamma / ^\circ$	90.000	90.000	90.000	90.000
Number of unit formulas per unit cell, Z	4	4	4	4
Volume / \AA^3	3686	3794	3775	3784
Calculated density / (g cm^{-3})	1.641	1.595	1.603	1.599
R_p	6.545	6.308	6.146	5.335
R_{wp}	11.025	9.683	10.115	8.510
χ^2	3.042	2.760	3.092	2.677

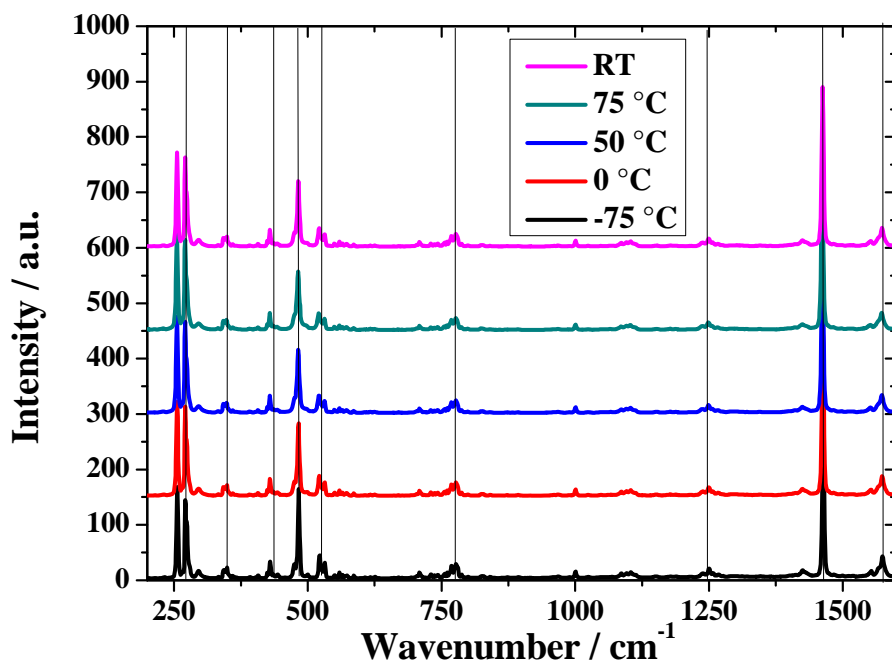


FIG. S5: Raman spectra at various temperatures (-75 °C, 0 °C, 50 °C, 75 °C, and room temperature [RT]). With the change in temperature no additional peaks or shifts were observed. Vertical lines are guides to the eye.

High-Temperature Properties of PCBM

No anomalous behaviour was observed by DSC in the temperature range from 180 to 210 °C (Fig. S6). At higher temperature endothermic events were noted as PCBM (powder and pellet) was heated (Fig. S6). Several thermal events were observed, and their temperatures and magnitudes ($\Delta_{\text{trs}}H$) depended on the sample morphology and the prior thermal treatment. In general, if heated sufficiently, there was a thermal event with an onset at ~ 240 °C, and also at ~ 280 °C. Both were endothermic on heating. See Table S4 for a summary. The lower-temperature event is most likely due to a polymorphic transition and was of lower magnitude (lower $\Delta_{\text{trs}}H$) for the pellet than for the powder. The second endothermic peak was due to melting and $\Delta_{\text{trs}}H$ due to this event was slightly larger for the pellet than for the powder. Although the

scanning rate (10 K min^{-1}) was rather high for highly accurate determination of the temperature of thermal events [17], it was chosen to optimize determination of $\Delta_{\text{trs}}H$, and it is clear from the results that the pellet undergoes a more substantial solid-solid transition than in the powder, but the overall change in entropy from the low-temperature solid to the liquid is about the same for both forms. On cooling, a broad exotherm was recorded for both samples, indicating sluggish crystallization.

Thermogravimetric analysis showed very small mass losses at $247 \text{ }^\circ\text{C}$ and $278 \text{ }^\circ\text{C}$ which might be due to adsorbed air or water (Fig. S7). At $\sim 400 \text{ }^\circ\text{C}$ the mass of PCBM decreased substantially as PCBM decomposed in air.

The PXRD pattern of a pellet of PCBM was recorded at room temperature after heating the pellet to $220 \text{ }^\circ\text{C}$, $260 \text{ }^\circ\text{C}$, and $290 \text{ }^\circ\text{C}$, respectively (Fig. S8). A change in structure was measured after heating to $220 \text{ }^\circ\text{C}$, which correlates with the first DSC peak and the increase in thermal expansion at $\sim 200 \text{ }^\circ\text{C}$. After heating to $290 \text{ }^\circ\text{C}$, the PXRD pattern showed two broad peaks, as the sample had been melted without recovering its original crystal structure (see DSC, Fig. S6).

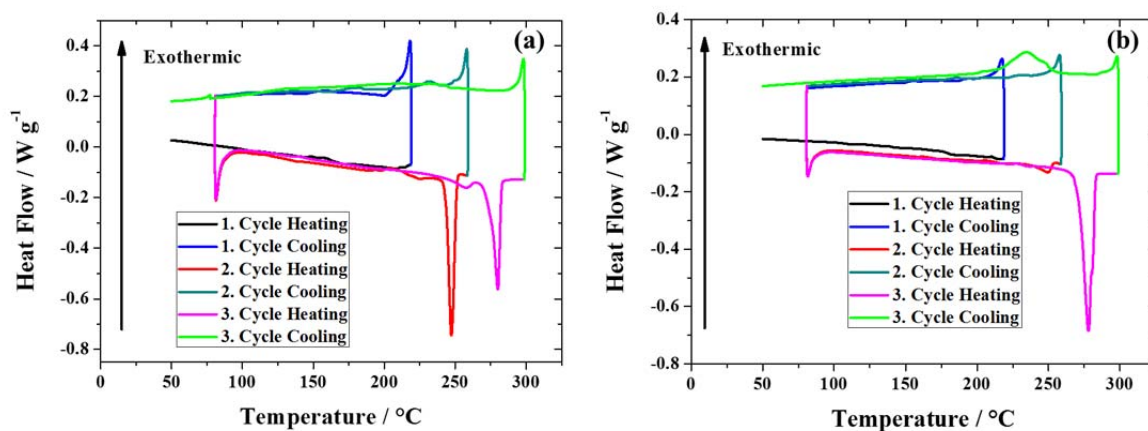


FIG. S6: DSC thermograms for (a) PCBM powder and (b) PCBM pellet. See Table S4 for onset temperatures, $\Delta_{\text{trs}}H$ and $\Delta_{\text{trs}}S$ values.

Table S4: Transition enthalpy change ($\Delta_{\text{trs}}H$), transition onset temperature (T_{trs}), and transition entropy change ($\Delta_{\text{trs}}S$) for the endothermic and exothermic peaks observed by DSC for PCBM powder and pellet.

Peak	$\Delta_{\text{trs}}H / \text{J g}^{-1}$	$T_{\text{trs}} / ^\circ\text{C}$	$\Delta_{\text{trs}}S / \text{mJ g}^{-1} \text{K}^{-1}$
POWDER:			
Heating 1. peak (endothermic)	18	244	35
Heating 2. Peak (endothermic)	15	275	27
Cooling 1. Peak (exothermic)	1.2	206	2.5
PELLET:			
Heating 1. Peak (endothermic)	1.7	240	3.3
Heating 2. Peak (endothermic)	24	278	44
Cooling 1. Peak (exothermic)	11	252	20

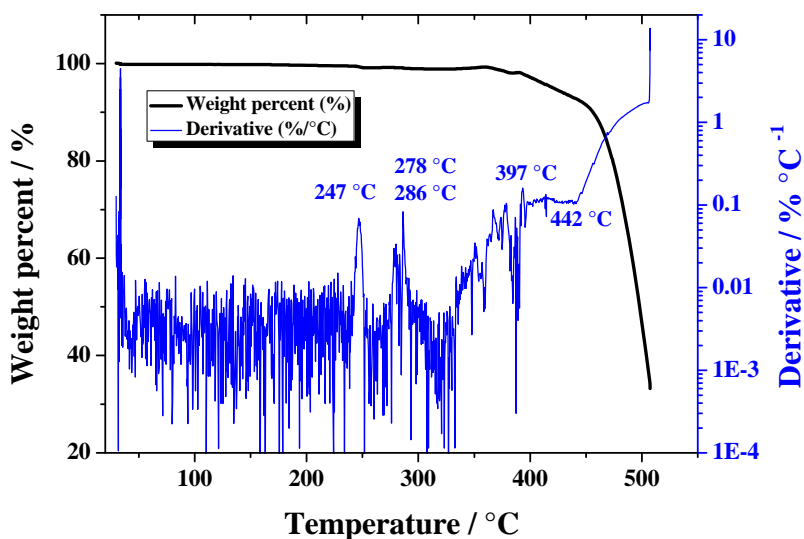


FIG. S7: Thermogravimetric analysis of PCBM powder. There is a small mass loss at 247 °C and 278 °C. Decomposition begins at ~400 °C in air.

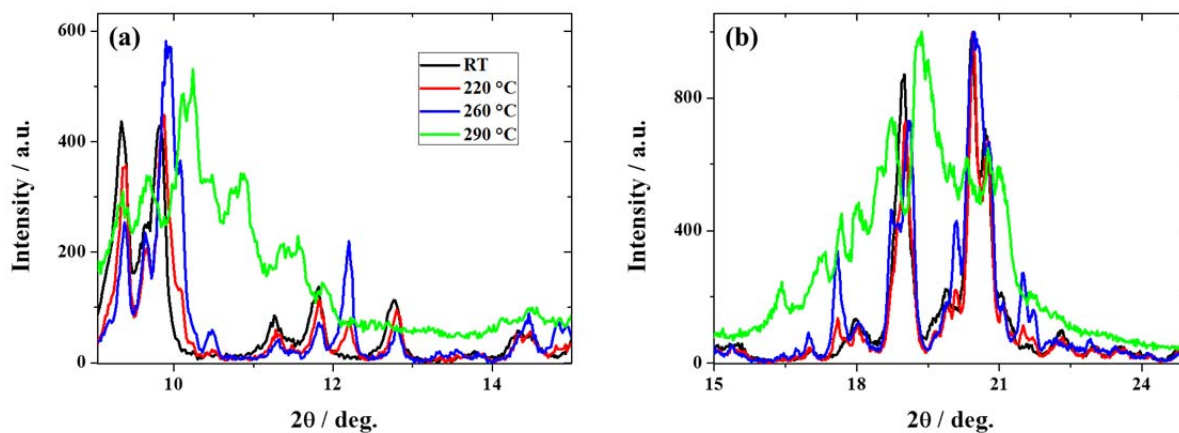


FIG. S8: PXRD pattern of PCBM at room temperature after heating to the temperatures indicated, at (a) low angle and (b) higher angle. Additional peaks were observed after heating to 220 °C and the intensity of the peaks increased after heating to 260 °C. After heating to 290 °C, two broad peaks were recorded.

Appendix: Experimental Data for PCBM

Table S5: Thermal Conductivity of a PCBM pellet.

T / K	$\kappa_{\text{Cycle1,Cooling}} / \text{mW m}^{-1} \text{K}^{-1}$	$\kappa_{\text{Cycle1,Heating}} / \text{mW m}^{-1} \text{K}^{-1}$	$\kappa_{\text{Cycle2,Cooling}} / \text{mW m}^{-1} \text{K}^{-1}$	$\kappa_{\text{Cycle2,Heating}} / \text{mW m}^{-1} \text{K}^{-1}$
383.5	-	77.8	-	-
363.5	-	73.9	73.4	-
323.5	-	67.6	66.4	-
304.4	67.6	65.1	64.8	-
252.9	63.7	59.7	61.8	-
204.4	63.0	56.4	59.8	-
168.9	62.5	55.7	59.0	-
136.3	63.0	57.9	58.7	54.8
108.3	63.4	58.3	59.5	55.9
78.0	63.8	60.4	60.7	58.0
59.8	64.9	62.3	61.7	59.9
43.5	65.1	63.7	62.3	61.6
29.4	63.8	63.1	61.1	-
20.2	59.0	58.6	-	-
14.2	51.2	51.1	-	-
7.4	34.1	33.4	-	-
4.5	22.2	22.2	-	-
2.0	8.95	-	-	-

Table S6: Heat capacity data: 1.908 mg; in order of data collection.

T / K	$C_p / \text{J mol}^{-1} \text{K}^{-1}$	T / K	$C_p / \text{J mol}^{-1} \text{K}^{-1}$	T / K	$C_p / \text{J mol}^{-1} \text{K}^{-1}$
303.74	737	53.26	98.4	9.94	17.3
283.42	661	48.25	91.0	9.00	14.7
263.27	611	43.71	84.8	8.16	12.2
243.02	554	39.59	78.9	7.39	10.0
222.82	496	35.87	73.1	6.71	8.267
202.58	438	32.50	67.8	6.08	6.47
182.29	386	29.44	62.1	5.50	5.09
162.07	326	26.68	57.4	4.98	3.95
141.86	272	24.17	52.1	4.51	2.97
121.63	225	21.90	47.4	4.09	2.18
101.42	180	19.84	42.6	3.70	1.55
96.35	168	17.98	38.5	3.35	1.12
87.25	147	16.29	34.2	3.03	0.77
79.07	137	14.76	30.5	2.75	0.52
71.64	125	13.37	26.8	2.49	0.34
64.89	115	12.11	23.4	2.25	0.23
58.78	106	10.97	20.3	2.04	0.15

Table S7: Heat capacity data: 3.210 mg; in order of data collection.

T / K	$C_p / \text{J mol}^{-1} \text{K}^{-1}$	T / K	$C_p / \text{J mol}^{-1} \text{K}^{-1}$	T / K	$C_p / \text{J mol}^{-1} \text{K}^{-1}$
304.70	718	48.52	93.4	9.07	15.3
284.25	665	43.96	87.0	8.22	12.8
264.04	607	39.83	80.6	7.44	10.5
243.77	553	36.09	74.9	6.76	8.70
223.53	498	32.70	69.2	6.12	6.90
183.00	386	29.62	63.8	5.54	5.47
162.71	329	26.85	58.3	5.01	4.20
142.43	277	24.34	53.4	4.54	3.22
122.14	228	22.04	48.4	4.11	2.40
101.90	184	19.97	43.7	3.72	1.76
96.82	172	18.08	39.3	3.37	1.26
87.70	152	16.39	35.2	3.05	0.88
79.47	142	14.86	31.3	2.76	0.60
72.02	129	13.46	27.7	2.50	0.41
65.24	118	12.20	24.2	2.26	0.27
59.10	109	11.06	21.0	2.05	0.18
53.55	101	10.02	17.9		

Table S8: Heat capacity data: 3.670 mg; in order of data collection.

T / K	$C_p / \text{J mol}^{-1} \text{K}^{-1}$	T / K	$C_p / \text{J mol}^{-1} \text{K}^{-1}$	T / K	$C_p / \text{J mol}^{-1} \text{K}^{-1}$
299.99	766	52.45	110	9.74	19.2
280.00	715	47.51	102	8.82	16.4
260.00	656	43.02	94.5	7.99	13.7
240.00	598	38.96	87.5	7.23	11.3
220.00	537	35.29	81.2	6.56	9.30
200.00	477	31.96	75.1	5.93	7.39
180.00	417	28.94	69.1	5.37	5.82
160.00	356	26.21	63.5	4.87	4.52
140.00	300	23.75	57.3	4.41	3.45
119.99	248	21.50	52.6	3.99	2.57
100.00	201	19.48	47.2	3.61	1.87
95.00	189	17.64	42.3	3.27	1.34
86.05	166	15.98	37.8	2.97	0.95
77.94	155	14.47	33.5	2.69	0.65
70.61	141	13.11	29.6	2.43	0.44
63.95	129	11.88	25.9	2.20	0.30
57.92	119	10.76	22.5	2.00	0.19

Table S9: Heat capacity data: 3.890 mg; in order of data collection.

T / K	$C_p / \text{J mol}^{-1} \text{K}^{-1}$	T / K	$C_p / \text{J mol}^{-1} \text{K}^{-1}$	T / K	$C_p / \text{J mol}^{-1} \text{K}^{-1}$
301.74	759	3.65	1.58	0.99	0.010
10.05	18.6	3.30	1.10	0.89	0.008
9.08	15.6	2.98	0.75	0.81	0.006
8.20	13.0	2.70	0.50	0.74	0.004
7.41	10.7	2.44	0.33	0.67	0.003
6.70	8.51	2.20	0.22	0.60	0.003
6.06	6.80	1.62	0.061	0.55	0.002
5.47	5.27	1.47	0.041	0.50	0.002
4.95	4.01	1.33	0.028	0.46	0.001
4.47	2.99	1.20	0.021	0.42	0.001
4.04	2.20	1.09	0.015	0.39	0.001

References

- [1] T. Erb, U. Zhokhavets, G. Gobsch, S. Raleva, B. Stühn, P. Schilinsky, C. Waldauf, and C. J. Brabec, *Adv. Funct. Mater.*, 2005, **15**, 1193.
- [2] M. Casalegno, S. Zanardi, F. Frigerio, R. Po, C. Carbonera, G. Marra, T. Nicolini, G. Raos, and S. V. Meille, *Chem. Commun.*, 2013 **49**, 4525.
- [3] R. Mens, P. Adriaensens, L. Lutsen, A. Swinnen, S. Bertho, B. Ruttens, J. D'Haen, J. Manca, T. Cleij, D. Vanderzande, and J. Gelan, *J. Polym. Sci. Pol. Chem.*, 2008, **46**, 138.
- [4] R. Mens, S. Chambon, S. Bertho, G. Reggers, B. Ruttens, J. D'Haen, J. Manca, R. Carleer, D. Vanderzande, and P. Adriaensens, *Magn. Reson. Chem.*, 2011, **49**, 242.
- [5] M. S. Dresselhaus, G. Dresselhaus, and P.C. Eklund, *J. Raman. Spectrosc.*, 1996, **27**, 351.
- [6] C. Yang, S. Cho, A. J. Heeger, and F. Wudl, *Angew. Chem. Int. Ed.*, 2009, **48**, 1592.
- [7] S. Falke, P. Eravuchira, A. Materny, and C. Lienau, *J. Raman Spectrosc.*, 2011, **42**, 1897.
- [8] C. Zhang, H. Chen, Y. Chen, Z. Wei, and Z. Pu, *Acta Phys.-Chim. Sin.*, 2008, **24**, 1353.
- [9] H.-H. Liu, S.-H. Lin, and N.-T. Yu, *Biophys. J.*, 1990, **57**, 851.
- [10] A. Einstein, *Ann. Phys.*, 1911, **35**, 679.
- [11] D. G. Cahill, S. K. Watson, and R. O. Pohl, *Phys. Rev. B*, 1992, **46**, 6131.
- [12] J. R. Olson, K. A. Topp, and R. O. Pohl, *Science*, 1993, **259**, 1145.
- [13] X. Yu, and D. M. Leitner, *Phys. Rev. B*, 2006, **74**, 184305.
- [14] L. Chen, X. Wang, and S. Kumar, *Sci. Rep.*, 2015, **5**, 12763.
- [15] P. Nagel, V. Pasler, S. Lebdkin, A. Soldatov, C. Meingast, B. Sundqvist, P.-A. Persson, T. Tanaka, K. Komatsu, S. Buga, and A. Inaba, *Phys. Rev. B*, 1999, **60**, 16920.
- [16] N.R. Tummala, S. Mehraeen, Y.-T. Fu, C. Risko, and J.-L. Brédas, *Adv. Funct. Mater.*, 2013, **23**, 5800.
- [17] Thermal Methods. M.B. Johnson and M.A. White, Chapter 2 in *Inorganic Materials: Multi Length-Scale Characterisation*; p. 63-119, D.W. Bruce, D. O'Hare and R. I. Walton, Editors. Wiley (2014).